Available online at www.sciencedirect.com
ScienceDirect
International Journal of Heat and Mass Transfer 50 (2007) 2394–2405
International Journal of HEAT and MASS TRANSFER
www.elsevier.com/locate/ijhmt

Multiple fluid flow and heat transfer solutions in a two-sided lid-driven cavity

W.-J. Luo [a], R.-J. Yang [b,*]

[a] Department of Electronic Engineering, Far East University, Tainan, Taiwan
[b] Department of Engineering Science, National Cheng Kung University, Tainan 70101, Taiwan

Received 19 February 2006; received in revised form 21 October 2006
Available online 18 December 2006

Abstract

This study presents a continuation method to calculate flow bifurcation with/without heat transfer in a two-sided lid-driven cavity with an aspect ratio of 1.96. The top and bottom lids of the cavity move in opposite directions and are allowed to be of different temperatures, thereby establishing a temperature gradient in the cavity flow and generating thermal transport. A comprehensive bifurcation diagram of the cavity flow is derived via the continuation method and linear stability analysis is used to identify the nature of the various flow solutions. For the isothermal flow case, the Reynolds number is used as the continuation parameter and three symmetric flows and two asymmetric flows are identified. For the non-isothermal flow case, the Grashof number is used as a continuation parameter. The flow evolution is studied for different temperature gradients, and bifurcation diagrams are constructed as a function of the continuation parameter. A thumb-shaped boundary line is established which identifies a restricted region defined in terms of the Grashof and Reynolds numbers within which a stable flow state exists.

Keywords: Vortex flows; Instabilities; Lid-driven cavity; Multiple solutions

1. Introduction

Flow in an enclosure driven by moving boundaries is a fundamental problem in fluid mechanics. This type of flow can be found in certain engineering applications within coating and drying technologies, or in academic research, where it may be used as a benchmark problem for testing various numerical methods and hydrodynamic stability problems. A classic example is the case where a flow is induced by the tangential movement of either one or both facing cavity boundaries (i.e. one-sided lid-driven cavity flow or two-sided lid-driven cavity flow, respectively). One-sided lid-driven flow in a square cavity was studied extensively in the literature. For example, the work by Pan and Acrivos [1], Prasad and Koseff [2], Ahlman et al. [3] and Croce et al. [4].

The one-sided lid-driven cavity flow problem was extended to the case of two-sided lid-driven cavity flow by Kuhlmann et al. [5,6]. These studies performed experimental and theoretical investigations into the two- and three-dimensional flows which are induced when the two facing sides of the cavity move with constant velocities in opposite directions to each other. Their results indicated that the existence of non-unique two-dimensional steady flows depends upon the cavity aspect ratio and upon the Reynolds number, which is determined by the wall velocities. At a low Reynolds number, the flow consists of separate co-rotating vortices adjacent to each of the moving walls. As the wall velocities increase, a jump transition occurs and the two vortices partially merge to generate a flow pattern which resembles cat's eyes. At high Reynolds numbers, the cat's eye flow becomes unstable and transforms into a steady three-dimensional cellular flow. Albensoeder et al.

* Corresponding author. Tel.: +886 6 275 7575x63343; fax: +886 6 276 6549.
E-mail address: rjyang@mail.ncku.edu.tw (R.-J. Yang).

0017-9310/$ - see front matter © 2006 Elsevier Ltd. All rights reserved.
doi:10.1016/j.ijheatmasstransfer.2006.10.025

[7] performed a numerical investigation of two-sided, lid-driven cavity flows and identified a large number of non-unique steady flow types. Alleborn et al. [8] investigated numerically two-dimensional flow accompanied by heat and mass transport in a two-sided lid-driven cavity containing a temperature gradient. Albensoeder et al. [9] provided accurate linear-stability boundaries, i.e. critical Reynolds number, for a wide range of aspect ratios and showed four different instabilities may occur which are all due to centrifugal effects. Albensoeder and Kuhlmann [10] investigated the linear stability of the cavity flow driven by two parallel moving walls with the same speed, and inquired about the type of instability and the dependence of the critical Reynolds and wave number on the aspect ratio. Albensoeder and Kuhlmann [11] investigated the flow driven by anti-parallel motion of two facing walls numerically, and showed the two-dimensional flow becomes unstable to different modes, depending on the cross-sectional aspect ratio. Blohm and Kuhlmann [12] measured the steady and time-dependent bifurcations which occur at higher Reynolds number. A review of the available literature shows that the flow transitions between multiple stable solutions in two-sided lid-driven cavity flow and the heat transfer in a cavity with a temperature gradient have not been discussed by previous researchers. For a systematic study of the respective instabilities and the non-linear pattern formation, the basic two-dimensional flow solutions must be known. Therefore, it is the purpose of this present study to investigate the stability of the two-dimensional solution manifold of such flows and to construct a complete chart of the heat transfer efficiency.

The governing equations for the resulting two-dimensional cavity flow are of a non-linear nature, and therefore, multiple solutions are possible. Previous numerical studies addressing the prediction of multiple stable solutions can be classified as belonging to one of two different approaches. The first approach treats the problem as an initial value problem and marches in time to attain a steady-state solution. The second approach solves the steady Navier–Stokes equations by means of a path following method or the so-called continuation method [13,14]. A disadvantage of the former approach is that it is generally unable to identify "steady-state unstable solutions" since the time-dependent Navier–Stokes equations will give a stable steady-state solution if its solution exists. Therefore it is difficult to justify genetic bifurcation patterns if using the time-marching method. However, the second approach is successful in determining both stable and unstable steady-state solutions [14,15]. Accordingly, it is this approach which the current study adopts to obtain a solution manifold and to construct bifurcation diagrams. A two-dimensional linear stability analysis is performed to determine whether or not each computed solution is stable. Once the solution manifold has been determined, a time-dependent formulation is developed in order to investigate the permissible flow transitions within the solution manifold.

The current study is summarized as follows: two-dimensional flow in a two-sided lid-driven cavity containing a temperature gradient is investigated numerically. The two lids are maintained at different temperatures and are moved tangentially in opposite directions to each other. The flow structures are highly dependent upon the aspect ratio of the cavity, which in the present study is 1.96, and upon the velocities of the two lids. By adopting the Reynolds number and the Grashof number as continuation parameters, flow transitions can be identified and bifurcation diagrams constructed as functions of the Reynolds number or of the Grashof number. The bifurcation diagrams illustrate the existent regions of various flow modes. Section 2 of this paper presents the governing equations for the two-sided lid-driven cavity flow with a temperature gradient and introduces the numerical method which will be adopted for its solution. Meanwhile, Section 3 presents the computed results and provides a detailed discussion. The final section of this paper presents some brief conclusions.

2. Governing equations and numerical method

2.1. Governing equations

Fig. 1 presents the case of an incompressible Newtonian fluid within a cavity whose height and width are given by H and L, respectively. In the present study, the aspect ratio of the cavity is defined as $H/L = 1.96$. The cooled upper wall is maintained at a constant temperature of T_c and moves at a velocity of U_b. Meanwhile, the constant temperature and velocity of the heated lower wall are given by $-U_b$ and T_h, respectively. The upper and lower walls move tangentially in opposite directions to each other. The stationary vertical walls are considered to be solid and adiabatic.

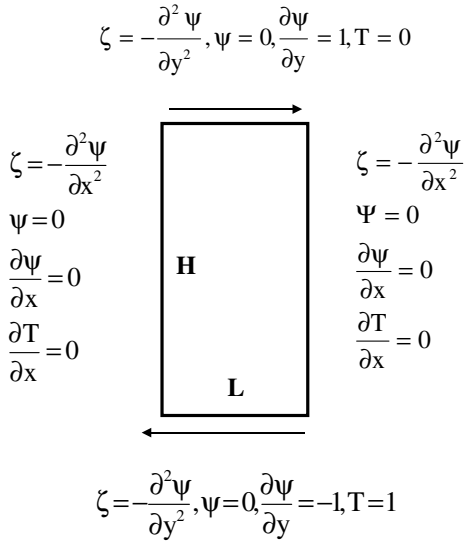

Fig. 1. The geometric model and boundary conditions of the cavity.

The non-dimensional governing equations in the Cartesian coordinate system for the stream function (ψ), vorticity function (ς) and thermal transport, respectively, can be written as

$$\frac{\partial^2\psi}{\partial x^2}+\frac{\partial^2\psi}{\partial y^2}=-\varsigma, \tag{1}$$

$$\frac{\partial\varsigma}{\partial t}+\frac{\partial\psi}{\partial y}\frac{\partial\varsigma}{\partial x}-\frac{\partial\psi}{\partial x}\frac{\partial\varsigma}{\partial y}=\frac{1}{Re}\left(\frac{\partial^2\varsigma}{\partial x^2}+\frac{\partial^2\varsigma}{\partial y^2}\right)-\frac{Gr}{Re^2}\left(\frac{\partial^2 T}{\partial y^2}\right), \tag{2}$$

$$\frac{\partial T}{\partial t}+\frac{\partial\psi}{\partial y}\frac{\partial T}{\partial x}-\frac{\partial\psi}{\partial x}\frac{\partial T}{\partial y}=\frac{1}{RePr}\left(\frac{\partial^2 T}{\partial x^2}+\frac{\partial^2 T}{\partial y^2}\right), \tag{3}$$

where T is the temperature of the fluid, $Re=U_bL/\nu$, $Gr=g\beta_T H^3(T_h-T_c)/\nu^2$, $Pr=\nu/\alpha$, ν is the kinematic viscosity of the fluid, g denotes the gravitational acceleration, β_T is the coefficient of thermal expansion and α is the thermal diffusivity. Note that for the isothermal flow case, the $Gr=0$ and hence the momentum equation is decoupled from the energy equation.

The boundary conditions of the cavity flow may be expressed as follows:

(a) On the top wall ($y=1.96$):

$$\psi=0,\quad \frac{\partial\psi}{\partial y}=1,\quad \frac{\partial\psi}{\partial x}=0,\quad \frac{\partial^2\psi}{\partial y^2}=-\varsigma,\quad T=0.$$

(b) On the bottom wall ($y=0$):

$$\psi=0,\quad \frac{\partial\psi}{\partial y}=-1,\quad \frac{\partial\psi}{\partial x}=0,\quad \frac{\partial^2\psi}{\partial y^2}=-\varsigma,\quad T=1.$$

(c) On the left-side wall ($x=0$):

$$\psi=0,\quad \frac{\partial\psi}{\partial y}=0,\quad \frac{\partial\psi}{\partial x}=0,\quad \frac{\partial^2\psi}{\partial x^2}=-\varsigma,\quad \frac{\partial T}{\partial x}=0.$$

(d) On the right-side wall ($x=1$):

$$\psi=0,\quad \frac{\partial\psi}{\partial y}=0,\quad \frac{\partial\psi}{\partial x}=0,\quad \frac{\partial^2\psi}{\partial x^2}=-\varsigma,\quad \frac{\partial T}{\partial x}=0.$$

To establish the steady solution manifold of the cavity flow, it is first necessary to drop the $\partial\varsigma/\partial t$ and $\partial T/\partial t$ terms from Eqs. (2) and (3).

The kinetic energy of the two-dimensional cavity flow is given by

$$\overline{Ke}=\frac{\int\int\left\{\left(\frac{\partial\psi}{\partial y}\right)^2+\left(\frac{\partial\psi}{\partial x}\right)^2\right\}\mathrm{d}x\,\mathrm{d}y}{\int\int\mathrm{d}x\,\mathrm{d}y}.$$

Owing to heat transfer feedback in the system, the local heat transfer coefficient, h, is expressed by the Nusselt number, which is defined below together with the average value of Nu:

$$Nu(x)=\frac{hH}{k}=-\left.\frac{\partial T}{\partial y}\right|_{y=0},$$

$$\overline{Nu}=\int_0^1 Nu(x)\,\mathrm{d}x.$$

2.2. Numerical method

The governing equations presented above are discretized by central differences of a second order in a regular grid system to form a system of non-linear algebraic equations, i.e.

$$G(X,\lambda)=0, \tag{4}$$

where X is the solution vector and λ is the continuation parameter, i.e. the Reynolds or Grashof number.

This gives an iterative sequence, $[X^{(\upsilon)}(\lambda)]$, which is expressed as

$$X^{(0)}(\lambda)\equiv\text{initial estimate}, \tag{5a}$$

$$G_X(X^{(\upsilon)},\lambda)[X^{(\upsilon+1)}-X^{(\upsilon)}]=-G(X^{(\upsilon)},\lambda),\quad \upsilon=0,1,2,\ldots \tag{5b}$$

where G_X is the Jacobian matrix of Eq. (4).

A suitable method of obtaining good initial estimates is to use a Taylor expansion of the solution with respect to changes in parameter λ, i.e.

$$X(\lambda+\delta\lambda)=X(\lambda)+\delta\lambda X_\lambda(\lambda). \tag{6a}$$

The solution vector, X_λ, is derived from Eq. (4) and satisfies the following:

$$G_X(X,\lambda)X_\lambda=-G_\lambda(X,\lambda). \tag{6b}$$

The iterative method described in Eqs. (5) and (6) is known as the Euler–Newton continuation. This method is extremely effective and usually converges quadratically. However, the method fails at points where the Jacobian matrix $G_X(X,\lambda)=0$ is singular. The Keller's continuation method [13] is introduced to overcome this difficulty, i.e.

$$N(X(s,\lambda(s)))\equiv\langle\dot{X}(s_0)\cdot[X(s)-X(s_0)]\rangle+\dot{\lambda}(s_0)[\lambda(s)-\lambda(s_0)]-(s-s_0)=0, \tag{7}$$

where $[X(s_0,\lambda(s_0))]$ is a previously computed solution for λ and $s=s_0$. $\dot{X}=\mathrm{d}X/\mathrm{d}s$ and $\dot{\lambda}=\mathrm{d}\lambda/\mathrm{d}s$ denote the components of a tangent vector to the solution path $[X(s),\lambda(s)]$.

A new system of equations can then be written as

$$\begin{cases}G(X,\lambda)=0,\\ N(X,\lambda,s)=0.\end{cases}$$

The Jacobian matrix of this new system is given by

$$\frac{\partial(G,N)}{\partial(X,\lambda)}=\begin{pmatrix}G_x & G_\lambda\\ N_x & N_\lambda\end{pmatrix}. \tag{8}$$

As well as the Keller's continuation method, it should be noted that with the Euler–Newton continuation in parameter s rather than in λ, it is also possible to follow the solution around singular points.

2.3. Linear stability analysis method

A linear stability analysis is performed in order to investigate the stability of the various flow states obtained by the continuation method described above. The basic state X_0

identified by Newton's method during continuation is perturbed by small, time-dependent quantities, i.e.

$$X = X_0 + \varepsilon e^{\gamma t}, \tag{9}$$

where ε is a small disturbance vector.

For transient solutions, a set of time-dependent equations can be derived and expressed as

$$M(X)\frac{dX}{dt} = G(X,\lambda), \tag{10}$$

where $M(X)$ is the mass matrix. This matrix is singular because some equations, e.g. the equation for stream function, do not possess an explicit time-dependent term.

Substituting Eq. (9) into Eq. (10), after collecting the linear terms of ε, gives the generalized algebraic eigenvalue problem, i.e.

$$\gamma M(X_0)\varepsilon = \widetilde{J}(X_0)\varepsilon. \tag{11}$$

where the matrix $\widetilde{J}$ represents the Jacobian matrix of $G(X,\lambda)$ evaluated for the basic state solution.

The stability characteristics of the basic state, X_0, is determined by the sign of the eigenvalue γ. The basic solution is infinitesimally stable if $Re\{\gamma\} < 0$ holds for all eigenvalues γ, i.e. if all perturbations in Eq. (9) decay with time. However, if at least one eigenvalue exists for which $Re\{\gamma\} > 0$, the corresponding eigenmode will grow as $t \to \infty$ and the basic solution is unstable. However, because M is singular, some eigenvalues are infinite and do not contribute towards linear instability. When calculating the leading eigenvalues, it is necessary to remove these infinite eigenvalues. An effective algorithm for doing so is a shift-and-inverse Arnoldi operation [16].

The generalized eigenvalue problem given in Eq. (11) can be transformed into a standard eigenvalue problem as follows:

$$(\widetilde{J} - \beta M)^{-1} M\varepsilon = \hat{\gamma}\varepsilon, \quad \hat{\gamma} = \frac{1}{\gamma - \beta}, \tag{12}$$

where β is a complex shift parameter such that $(\widetilde{J} - \beta M)^{-1}M$ is not singular.

This standard problem is then solved by a restarted, iterative Arnoldi method, which is essentially a sophisticated extension of the power iteration method and which allows a number of eigenvalues $\hat{\gamma}$ of largest magnitude to be calculated. ARPACK [16,17]. an Arnoldi-method based package, is then used to calculate the leading eigenvalues and corresponding eigenvectors.

The identification of flow transitions between various flow modes is implemented by backwards-Euler time stepping. The governing equations are discretized according to the following scheme:

$$G(X,t) = 0. \tag{13}$$

This gives a sequence of iteration $[X^{(\upsilon)}(t)]$ which is defined by

$$X^{(0)}(0) \equiv \text{initial state}, \tag{14a}$$

$$G_X(X^{(\upsilon)},t)[X^{(\upsilon+1)}(t+\Delta t) - X^{(\upsilon)}(t+\Delta t)] = -G(X^{(\upsilon)},t), \quad \text{where } \upsilon = 0,1,2,\ldots \tag{14b}$$

In Eq. (14b), G_X is the Jacobian matrix of Eq. (13).

An effective method to obtain good initial estimates for this calculation is to employ a Taylor expansion of the solution with respect to changes in the parameter Δt, i.e.

$$X^{(0)}(t + \delta(\Delta t)) = X(t) + \delta(\Delta t)X_t(t). \tag{15}$$

Eq. (13) is used to obtain X_t, and it satisfies:

$$G_X(X,t)X_t = -G_t(X,t). \tag{16}$$

The method described in Eqs. (14)–(16) is known as the backwards-Euler time stepping. Since the second order accuracy in time is employed, it is necessary to provide two initial solutions at the beginning of the time marching calculation. One of these solutions can be obtained from the initial stable state, while the other is obtained by using the same numerical method with a first order finite difference in time. Before the iteration algorithm is executed in order to obtain the convergence solution of the next time level, a predictor step is applied which yields close estimates to the convergence solution. Hence, the calculation algorithm is extremely effective and usually the method has quadratic convergence in numerics.

3. Results and discussion

3.1. Isothermal flow case using Re as the continuation parameter

A two-dimensional steady incompressible isothermal flow ($Gr = 0$) in a rectangular cavity with an aspect ratio of 1.96 is calculated. The 2-D basic flow is computed using a second-order finite difference method with grid stretching towards all boundaries. In comparison to the results computed by doubled resolution on 181×281 grid points, grid independent solutions are practically obtained by 91×141 non-equal space grid points. The 91×141 grid points are employed for all calculations. The flow is driven by the upper and lower cavity walls, which move with equal velocities in opposite directions. The Reynolds number of the flow is proportional to the wall velocities. The continuation method is used to predict the two-vortex flow and the cat's eye flow, which occur at $Re = 200$ and $Re = 240$, respectively. Fig. 2 compares the present theoretical results for the horizontal velocity component distributions of the flows along the plane which intersects the middle of the upper and lower walls with experimental results by Kuhlmann et al. [5]. It is clear that there is good agreement between the two sets of results. Fig. 3a plots the value of the stream function at the cavity center as a function of the Reynolds number. It is noted that the continuation

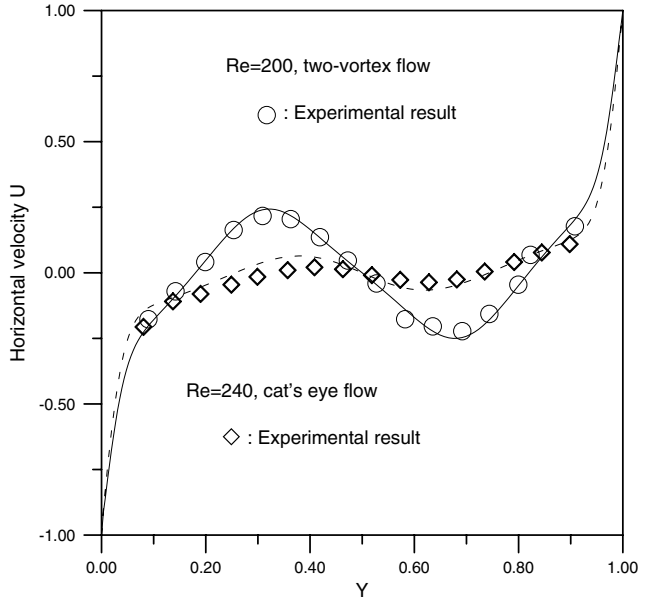

Fig. 2. The horizontal velocity U-Component distribution of present results compared with that of experimental results [5].

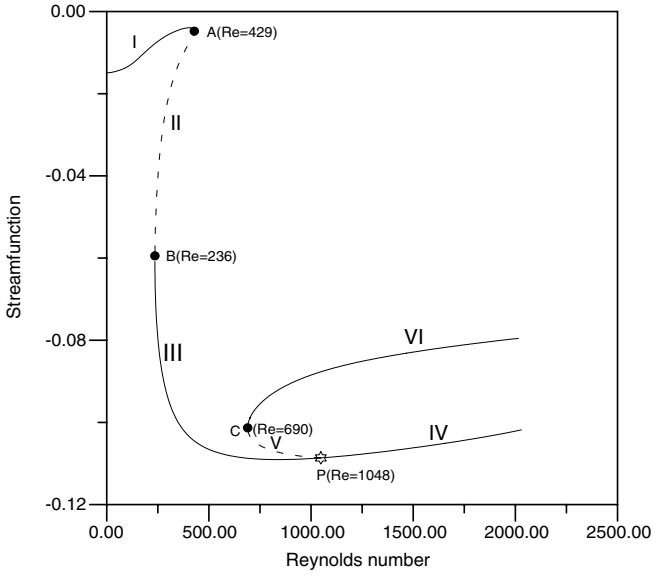

Fig. 3a. The stream function value at the cavity center traced by *Re*, point A, B and C are saddle-node points, point P is a pitch-fork bifurcation point, the flows in segment II, V are unstable and others are stable.

curve comprises six individual segments. Along segment I, the flow remains stable as the Reynolds number increases from a low value to a critical value of $Re = 429$, which is marked as point A and which represents a saddle-node bifurcation. Along the continuation path from points A to B (i.e segment II), the flow becomes unstable until $Re = 236$ (point B), at which point a second saddle-node bifurcation is evident. Along segment III, the flow becomes stable once again until point P, which occurs at a value of $Re = 1048$ and which represents a symmetry-breaking bifurcation point. After point P, segment III divides into two separate segments, i.e. segment IV and segment V. Flows in segment IV inherit the stable flow characteristics evident in segment III, while the flow in segment V exhibits an unstable asymmetry state which persists until point C ($Re = 690$), at which point a third saddle-node bifurcation is identified. After point C, the flow in segment VI is more asymmetrical and exhibits stable characteristics. In previous studies, Kuhlmann et al. [5,6] identified the two bifurcation points noted at points A and B and cited corresponding *Re* values of 427 and 234, respectively. It is noted that the current theoretically predicted values of 429 and 236 are in good agreement with these published results. The symmetry-breaking bifurcation point (point P) has not been reported previously, however. The present theoretical results clearly indicate the existence of multiple flow solutions in the regions of $Re = 236$–429, $Re = 690$–1048 and $Re = 1048$–2000.

Fig. 3b plots the value of the two-dimensional cavity flow kinetic energy, $\overline{Ke}$, as a function of the Reynolds number. Along segment I, the kinetic energy of the flow increases with rising Reynolds number, which is proportional to the driving momentum of the walls. The flow then undergoes a saddle-node bifurcation at point A, corresponding to $Re = 429$. Along segment II of the continuation path (i.e. from points A to B), it is observed that the kinetic energy of the unstable flow reduces significantly as *Re* falls to a value of 236. The reduction of the kinetic energy means that the cat's eye flow requires less supplied energy to sustain itself. Subsequently, the kinetic energy increases gradually as the Reynolds number rises to a value of $Re = 1048$ (i.e. point P), which represents a symmetry-breaking bifurcation point. At point P, segment III divides into segments IV and V. The flow along segment

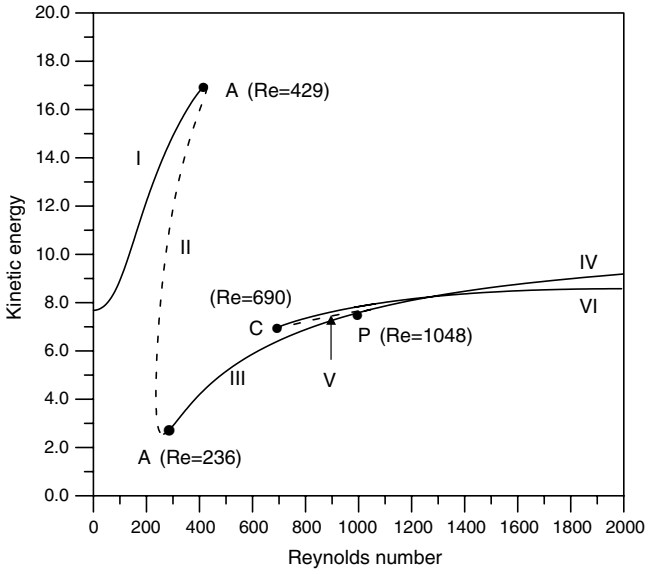

Fig. 3b. The kinetic energy of the cavity flow traced by *Re*, point A, B and C are saddle-node points, point P is a pitch-fork bifurcation point, the flows in segment II, V are unstable and others are stable.

V undergoes a saddle-node bifurcation at point C. In general, the kinetic energy of the flow increases slowly with an increase of Reynolds number. It should be noted that the intersection point of the kinetic energy distributions of segments IV and VI does not represent a bifurcation point.

Fig. 4 depicts the streamline contours of the predicted flow patterns along the continuation path. The upper cavity wall moves towards the right, while the lower wall moves in the opposite direction with an equal velocity. The flow develops from a low Reynolds number along segment I of the continuation path. Two separate vortices are apparent adjacent to each of the moving walls and a stagnation point appears at the center of the cavity. Both vortices co-rotate in a clockwise direction and their strength increases as the Reynolds number rises. This flow pattern is referred to as two-vortex flow by Kuhlmann et al. [5]. Two small recirculations located approximately midway between the upper and lower walls appear next to the stationary cavity walls. These two recirculations expand in size as the *Re* number increases and result in a "pinch effect" of the two co-rotating vortices. At point A, which corresponds to a value of $Re = 429$, the two co-rotating vortices merge slightly. As the Reynolds number decreases along segment II, the two recirculations become smaller and finally vanish at point B ($Re = 236$), where it is noted that the two co-rotating vortices are partially merged. This flow mode is referred to by Kuhlmann et al. [5] as "cat's eye flow". Along segment III which originates from point B, the two co-rotating vortices finally merge to form a single large recirculation which occupies most of the cavity. As the Reynolds number increases, two small recirculation bubbles appear in the top-left and bottom-right corners of the cavity. As shown in Fig. 4(b), these bubbles gain in strength along segment IV. Segments V and VI represent the asymmetric flows which originate from the symmetry-breaking bifurcation point, P. Along segment V, one of the small bubbles gains in size and strength and causes the other bubble to decay. As indicated in Fig. 4(c), only the small bubble in the top-left corner of the cavity survives. This phenomenon causes the flow to become asymmetrical. Along segment VI, the surviving small bubble expands rapidly and suppresses the major recirculations in the center of the cavity. Meanwhile, another small recirculation appears in the bottom-right cavity corner.

3.2. Flow transition

The bifurcation diagram constructed in Fig. 3 not only illustrates the restricted ranges of Reynolds number for which equilibrium flow states exist, but also provides information about the permissible flow transitions and the final flow state. It clearly indicates multiple solutions in the

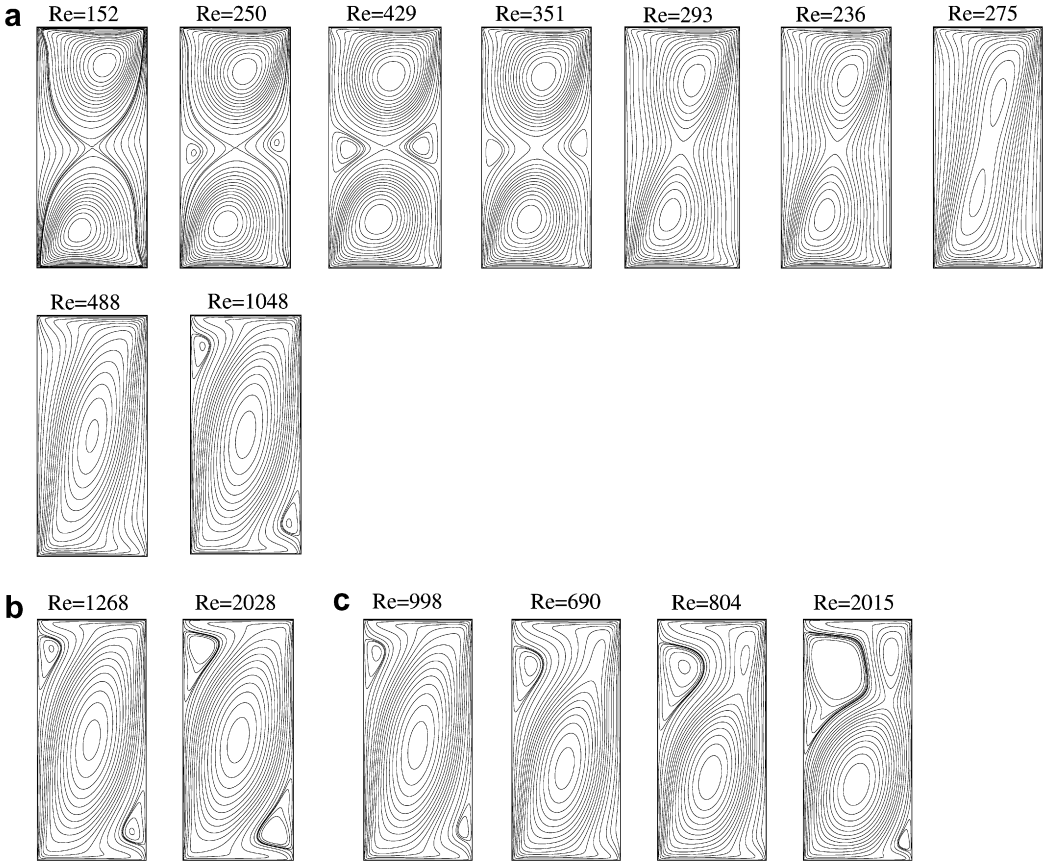

Fig. 4. The flow patterns in each branch: (a) Follow segment I, II and III to the pitch-fork point ($Re = 1048$), (b) symmetric flow patterns after the pitch-fork point along segment IV and (c) the development of asymmetric flow patterns after the pitch-fork point along V and VI.

regions of $236 < Re < 429$, $690 < Re < 1048$ and $Re > 1048$, respectively. A time-stepping numerical method can be applied to generate the time-dependent transitions among the stable states. Since the initial-value solver is inherently unable to converge to unstable solutions, it is only possible to obtain stable equilibrium at specific Reynolds numbers if it converges in time. The permitted stable flow states can be generated by an appropriate control of the upper and lower cavity wall velocities, i.e. by controlling the Reynolds number of the flow. This transition process not only provides information about flow evolution, but also confirms flow stability. A few examples are listed in the following:

3.2.1. Two-vortex flow to cat's eye flow transition

The transition from two-vortex flow to cat's eye flow is generated by commencing with a stable two-vortex flow and then suddenly accelerating the two walls to a range of $429 < Re < 690$ such that only the cat's eye flow remains stable. Fig. 5 shows a typical example of the flow transition. It is noted that although stable cat's eye flow also exists when $Re > 236$, the two-vortex flow to cat's eye flow transition can only occur in the range of $429 < Re < 690$. When $Re > 690$, two stable flows (i.e. cat's eye flow and strong asymmetric flow) exist. Therefore, suddenly accelerating the speed to this range cannot guarantee a transition to cat's eye flow, i.e. the terminal state may either be a cat's eye flow or a strong asymmetric flow.

3.2.2. Cat's eye flow to two-vortex flow transition

The cat's eye flow to two-vortex flow transition is generated by commencing with a stable cat's eye flow and then suddenly decelerating the wall velocities to a range of $Re < 236$ such that only the two-vortex flow remains stable. Fig. 6 shows the flow transition by reducing Re from 600 to 200. Note that although the stable two-vortex flow actually exists when $Re < 429$, a flow transition to a two-vortex flow can only be guaranteed when $Re < 236$, because in the range $236 < Re < 429$, two stable flows co-exist (i.e. cat's eye flow and two-vortex flow) and the final flow solution cannot be predicted.

3.2.3. Strong asymmetric flow to two-vortex flow transition

A strong asymmetric flow to two-vortex flow transition can be generated by commencing with a stable strong asymmetric flow and then suddenly decelerating the velocities of the two driving walls to a range of $Re < 236$ such that only the two-vortex flow remains stable. Fig. 7 illustrates the flow transition by reducing Re from 866 to 200.

3.2.4. Strong asymmetric flow to cat's eye flow transition

The strong asymmetric flow to cat's eye flow transition can be generated by commencing with a stable strong asymmetric flow and then suddenly decelerating the driving velocities of the upper and lower cavity walls to a range of $429 < Re < 690$ such that only the cat's eye flow is stable. Fig. 8 shows an example of the flow transition by reducing Re from 866 to 600. Although stable cat's eye flow exists when $Re > 236$, only in the range $429 < Re < 690$ can the strong asymmetric flow be guaranteed to evolve into cat's eye flow. When $Re > 690$, two stable states are evident, i.e. strong asymmetric flow and cat's eye flow. Either

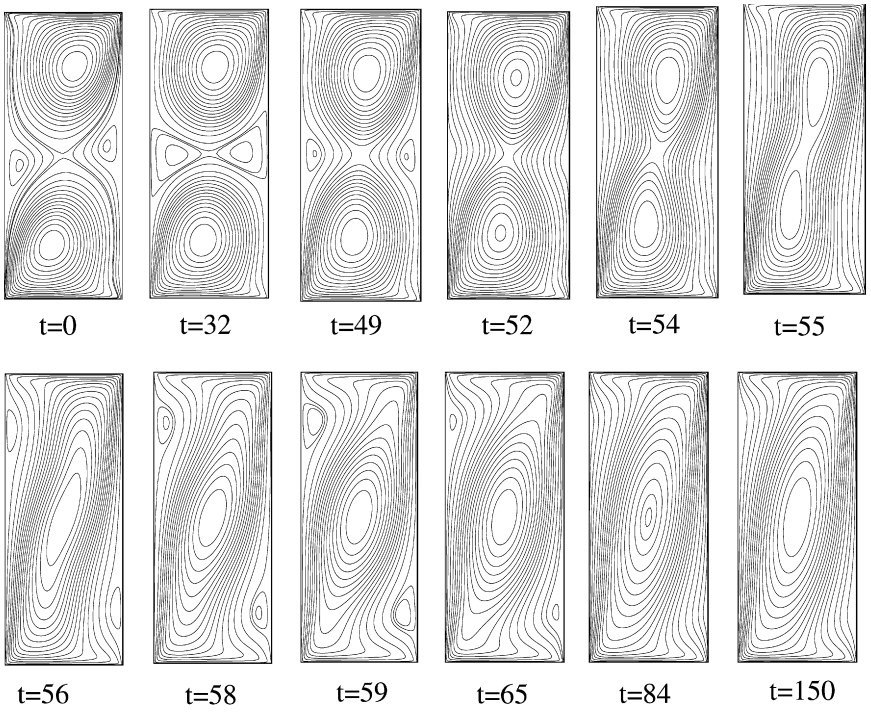

Fig. 5. The flow evolution of constant stream-function contour during two-vortex flow to cat's eye flow transition by increasing Re from 200 to 600.

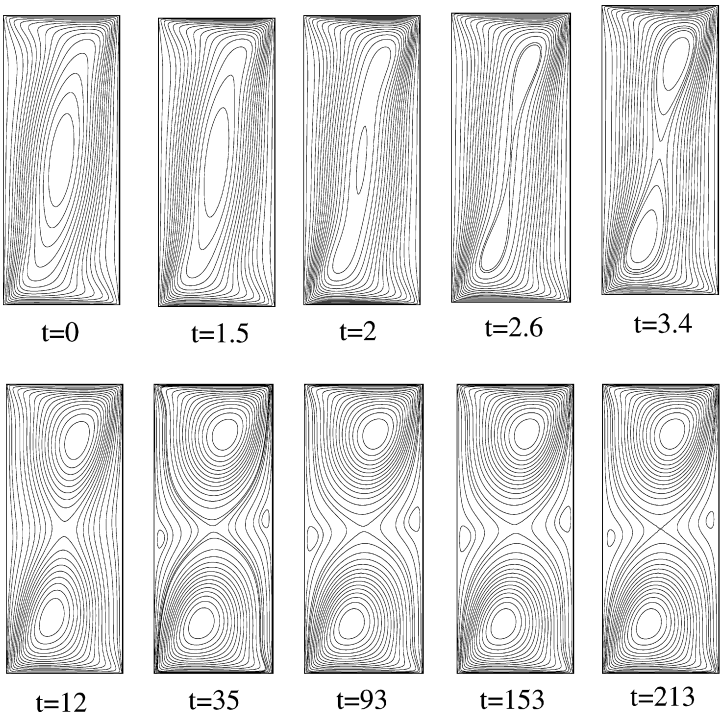

Fig. 6. The flow evolution of constant stream-function contour during cat's eye flow to two-vortex flow transition by reducing *Re* from 600 to 200.

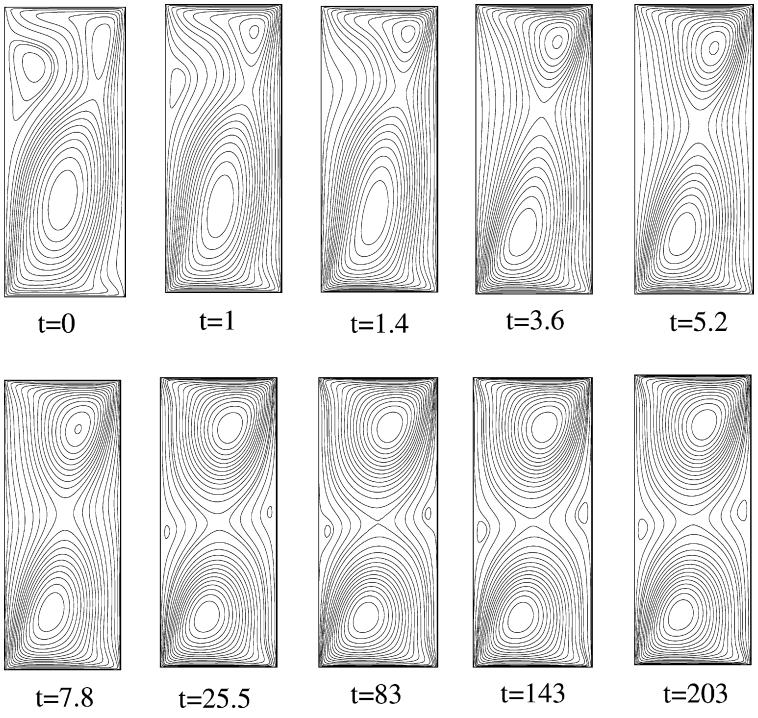

Fig. 7. The flow evolution of constant stream-function contour during strong asymmetric flow to two-vortex flow transition by reducing *Re* from 866 to 200.

decelerating or accelerating the driving velocities to this range will result in a terminative cat's eye or asymmetric flow. Furthermore, the range $236 < Re < 429$ also generates two stable flow states, i.e. two-vortex flow and cat's eye flow. Therefore, decelerating the upper and lower walls to this range will not guarantee a transition to cat's eye flow. In fact, the terminative flow state depends on the deceleration history of the two walls.

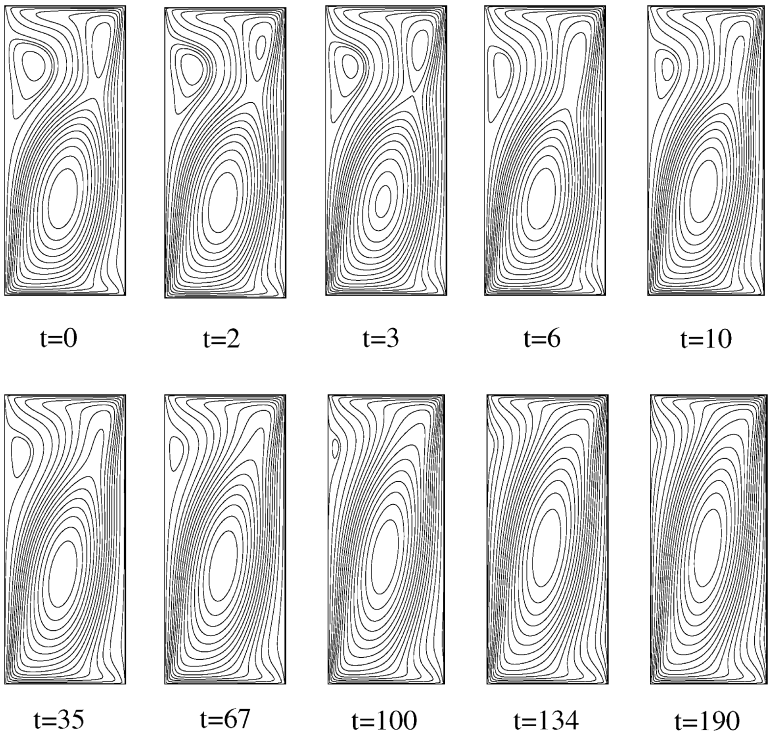

Fig. 8. The flow evolution of constant stream-function contour during strong asymmetric flow to cat's eye flow transition by reducing *Re* from 866 to 600.

3.3. Non-isothermal flow case using Gr as the continuation parameter

In addition to moving the upper and lower cavity walls in opposite directions at the same velocity, the flow may also be driven by the temperature gradient within the cavity. The change in fluid density caused by the temperature gradient is governed by the Boussinesq approximation. A continuation method is used to compute flow solutions and we plot the values of the average Nusselt number as a function of the Grashof number for several values of Reynolds numbers in the range $Re \leqq 600$. As shown in Fig. 9, when $Re < 195$, no saddle-node bifurcation points are apparent and consequently the flow states on these branches are stable. However, when $Re \geqq 195$, two saddle-node bifurcation points are identified on the corresponding branches and an unstable flow state is found to appear between the two points. If these points are connected, they form a thumb-shaped boundary line. The flow states outside the boundaries of this line are stable, while those within the boundary are unstable. The saddle-node bifurcation points located on specific branches can be used to distinguish the regions of stability and instability as functions of the Reynolds and Grashof numbers. If these branches are followed from a lower Grashof number, it is observed that these saddle-node points destabilize the initially stable cat's eye flow. The resulting unstable flow is subsequently stabilized by a further saddle-node point and becomes a stable two-vortex flow. As an example, Fig. 10 shows the streamline patterns and isothermal contours as a function of Grashof number for $Re = 350$. With

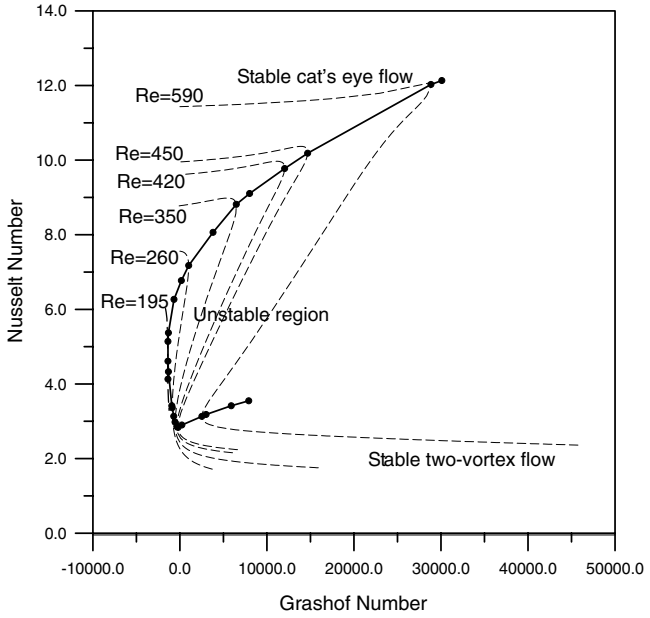

Fig. 9. The stability distribution in the cavity flow.

an increase in the Grashof number, the temperature gradient causes hot fluid near the lower cavity wall to move upwards and cool fluid near the upper wall to move downwards within the large recirculation associated with cat's eye flow. Therefore, a convection effect is gradually developed in the cavity. Subsequently, the streamline contours gradually pinch at a midway point between the upper and lower walls to form a stagnation point at the cavity

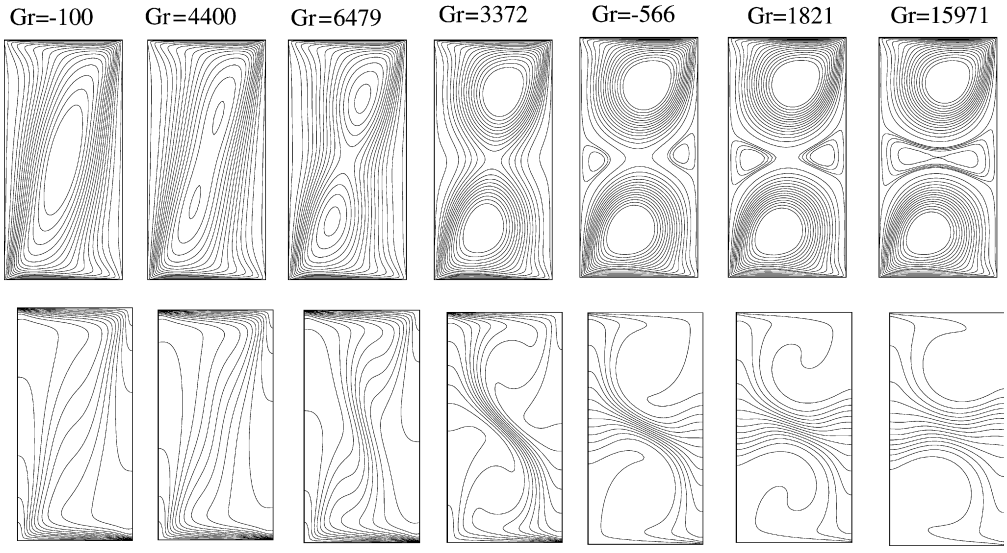

Fig. 10. The streamline contours and isothermal lines traced by Gr for $Re = 350$.

center. As shown in Fig. 10, most isothermal lines adjacent to the upper and lower walls transfer a significant amount of heat energy to the two walls. The cat's eye flow cannot sustain an excessive flow convection in the cavity and eventually becomes destabilized by a saddle-node bifurcation point at $Gr = 6479$. After the saddle-node point, the pinch effect midway between the two moving walls gradually becomes more pronounced as the Grashof number decreases. Two recirculations appear in close proximity to the adiabatic sides of the cavity and two separate co-rotating vortices are gradually formed in place of the large recirculation. These vortices prevent the adequate mixing of the hot rising fluid and the cool sinking fluid with the result that there is a significant decrease in the heat transferred on the lower cavity wall. The unstable flow becomes stabilized through a second saddle-node bifurcation point at $Gr = -566$ and the two co-rotating vortices gradually separate. The negative value of the Grashof number indicates the case where the temperature of the upper wall is higher than that of the lower one. As the Grashof number increases, these two vortices become more coherent. Furthermore, most of the isothermal lines are concentrated towards the center of the cavity, which implies that the heat transfer on the bottom wall continues to be inefficient. It is noted that the multiple solutions identified with changes in the Grashof number correspond well to the branches

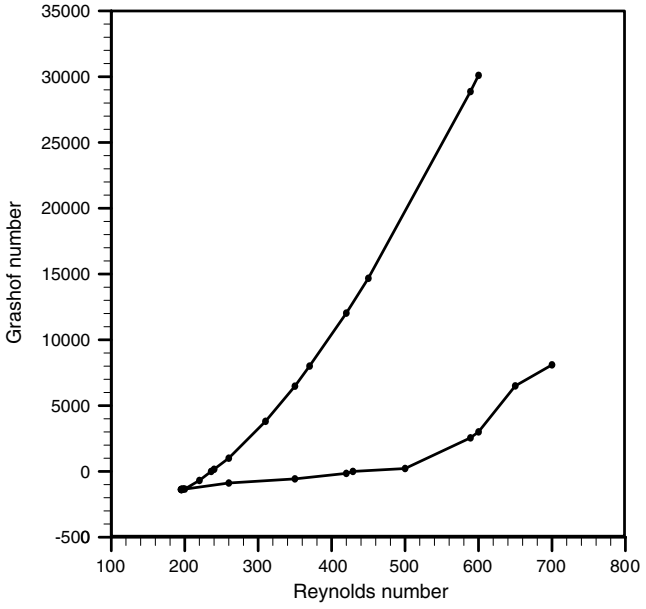

Fig. 11. The distribution of saddle-node bifurcation points as functions of the Reynolds number and the Grashof number.

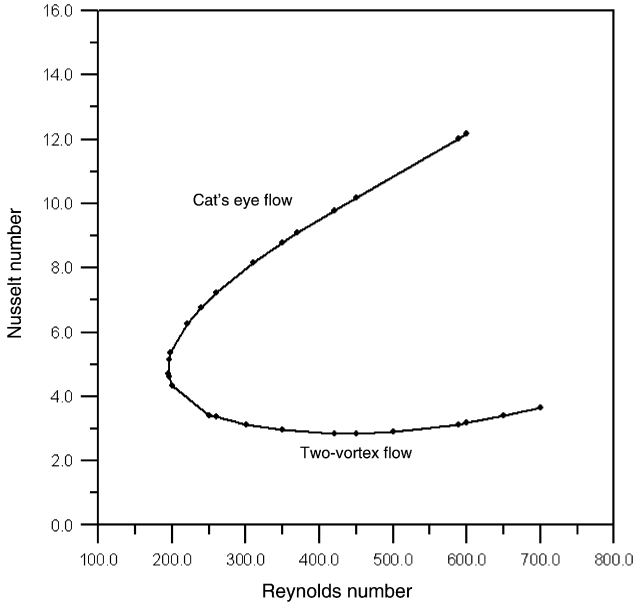

Fig. 12. The distribution of saddle-node bifurcation points as functions of the Reynolds number and the Nusselt number.

plotted previously when using the Reynolds number as the continuation parameter.

Fig. 11 shows the distribution of saddle-node bifurcation points as functions of the Reynolds number and the Grashof number. Two boundary lines can be used to distinguish the existent region of each flow. The cat's eye flow exists in the region below the upper line, however the two-vortex flow exists in the region above the lower line. Both flow states coexist between the two boundary lines. Fig. 12 shows the distribution of saddle-node bifurcation points as functions of the Reynolds number and the Nusselt number. When $Re \geqq 195$, two saddle-node bifurcation points exist for each Reynolds number. The flow at the upper point is cat's eye flow, and the flow at the lower point is two-vortex flow.

4. Conclusions

The present study has presented the use of a continuation method to predict the multiple flow solutions for a two-sided lid-driven flow with/without heat transport. This type of flow can be found in many applications within the coating and drying technologies field.

For the case without heat transfer, using the Reynolds number as a continuation parameter, five distinct flow solutions have been calculated within the considered parameter range (i.e. $Re < 2000$) and a comprehensive bifurcation diagram has been constructed. The bifurcation diagram is a useful means of revealing the physics of the flow and can be used to identify the region of stable solutions and the relations between these solutions. Three of the five calculated solutions are determined to be stable. Of these, two solutions are symmetric while the remaining solution is asymmetric. The asymmetric solution branch which originates from a symmetry-breaking pitchfork bifurcation is stabilized by a subsequent saddle-node bifurcation resulting in the eventual formation of a strong asymmetric flow. A new bifurcation point is identified from these solutions, namely, the symmetry-breaking bifurcation point P at $Re = 1048$. In comparison to the 3-D results shown in [9,11], the present 2-D results show the region of multiplicity is mostly beyond the border of stability against 3-D perturbations. Most of the flow states shown in Section 3.1 cannot be realized in an experiment, only the two-vortex flow and the cat's eye flow is stable against 3-D perturbations.

Time-dependent calculations have also been performed to study the flow transitions between various stable flows. By controlling the velocities of the upper and lower walls (i.e. the Reynolds number), the flow within the cavity can be led through its permitted stable states. The constructed bifurcation diagram not only illustrates the restricted Reynolds number ranges within which equilibrium states can exist, but also illustrates the permissible transitions between them and indicates the eventual terminative flow state. The transition process provides valuable information regarding flow evolution and can be used to confirm flow stability.

The study has also considered the use of the Grashof number as a continuation parameter for the case with heat transfer and has plotted a series of flow branches for different values of Reynolds number. It has been shown that a unique stable solution exists at lower Reynolds numbers. For higher values of Reynolds number, two saddle-node points are identified on the corresponding branches and it has been noted that the flow states between the two saddle-node points become unstable.

Finally, it has been demonstrated how connecting these saddle-node bifurcation points forms a thumb-shaped boundary line which separates the stable flow states from the unstable states, i.e. the boundary line identifies the restricted range of Reynolds and Grashof number within which stable states may be attained. This information is highly valuable when designing industrial applications.

Acknowledgements

This work has been supported by the R.O.C. National Science Council under grant numbers NSC 91-2212-243-001. We thank Mr. Wen-Tsou Lee for executing a few flow calculations and Professor Sorensen of Rice University for making ARPACK available.

References

[1] F. Pan, A. Acrivos, Steady flows in rectangular cavities, J. Fluid Mech. 28 (1967) 643–655.
[2] A.K. Prasad, J.R. Koseff, Reynolds number and end-wall effects on a lid-driven cavity flow, Phys. Fluids A 1 (1989) 208–218.
[3] D. Ahlman, F. Soderlund, J. Jackson, A. Kurdila, W. Shyy, Proper orthogonal decomposition for time-dependent lid-driven cavity flows, Numer. Heat Transfer, Part B: Fundam. 42 (4) (2002) 285–306.
[4] G. Croce, G. Comini, W. Shyy, Incompressible flow and heat transfer computations using a continuous pressure equation and nonstaggered grids, Numer. Heat Transfer, Part B: Fundam. 38 (3) (2002) 291–307.
[5] H.C. Kuhlmann, M. Wanschura, H.J. Rath, Flow in two-sided lid-driven cavities: non-uniqueness, instabilities, and cellular structures, J. Fluid Mech. 336 (1997) 267–299.
[6] H.C. Kuhlmann, M. Wanschura, H.J. Rath, Elliptic instability in two-sided lid-driven cavity flow, Eur. J. Mech. B/Fluids 17 (1998) 561–569.
[7] S. Albensoeder, H.C. Kuhlmann, H.J. Rath, Multiplicity of steady two-dimensional flows in two-sided lid-driven cavities, Theor. Comp. Fluid Dyn. 14 (2001) 223–241.
[8] N. Alleborn, H. Raszillier, F. Durst, Lid-driven cavity with heat and mass transport, Int. J. Heat Mass Transfer 42 (1999) 833–853.
[9] S. Albensoeder, H.C. Kuhlmann, H.J. Rath, Three-dimensional centrifugal-flow instabilities in the lid-driven-cavity problem, Phys. Fluids 13 (2001) 121–135.
[10] S. Albensoeder, H.C. Kuhlmann, Three-dimensional instability of two counter-rotating vortices in a rectangular cavity driven by parallel wall motion, Eur. J. Mech. B/Fluids 21 (2002) 307–316.
[11] S. Albensoeder, H.C. Kuhlmann, Linear stability of rectangular cavity flows driven by anti-parallel motion of two facing walls, J. Fluid Mech. 458 (2002) 153–180.
[12] C. Blohm, H.C. Kuhlmann, The two-sided lid-driven cavity: experiments on stationary and time-dependent flows, J. Fluid Mech. 450 (2002) 67–95.

[13] H.B. Keller, Numerical Solution of Bifurcation and Nonlinear Eigenvalue Problems, Applications of Bifurcation Theory, Academic Press, 1977, p. 359.
[14] R.-J. Yang, W.-J. Luo, Flow bifurcations in a thin gap between two rotating spheres, Theor. Comp. Fluid Dyn. 16 (2002) 115–131.
[15] W.-J. Luo, R.-J. Yang, Flow bifurcation and heat transfer in a spherical gap, Int. J. Heat Mass Transfer 43 (2000) 885–899.
[16] D.C. Sorensen, Implicit application of polynomial filters in a k-step Arnoldi method, SIAM (Soc. Ind. Appl. Math.) J. Matrix Anal. Appl. 13 (1992) 357.
[17] Y. Saad, Numerical Methods for Large Eigenvalues Problems, Halsted Press, New York, 1992.